ELSEVIER

Materials Science and Engineering A 435–436 (2006) 698–704

MATERIALS SCIENCE & ENGINEERING A

www.elsevier.com/locate/msea

Creep behavior of Ti–40Al–10Nb titanium aluminide intermetallic alloy

Chau-Jie Zhan, Tso-Hao Yu, Chun-Hao Koo *

Department of Materials Science and Engineering, National Taiwan University, No. 1, Sec. 4, Roosevelt Road, Taipei 106, Taiwan, ROC

Received 1 December 2005; received in revised form 24 July 2006; accepted 26 July 2006

Abstract

The microstructure and creep behavior of the Ti–40Al–10Nb alloy processed by conventional hot rolling has been investigated. By means of heat treatment, the microstructure of the alloy could be controlled. The experimental result shows that the creep resistance of the alloy is strongly affected by its microstructure. The structure of Widmanstätten lath has more creep resistance than that of the lamellar grain one. The increased creep properties by the structure of Widmanstätten lath is owing to the short mean free path of the dislocation slip. Most of the creep performance of the alloy is dominated by the tertiary creep. The creep curve of the alloy does not show an extended steady-state region, which is associated with the lack of a distinct subgrain substructure during creep. The creep deformation of the alloy for the secondary creep stage mainly converges in the B2 phase. The estimated stress exponent, which is three, reveals that the creep mechanism is controlled by dislocation glide and climb. The calculated activation energy for the structure of Widmanstätten lath and lamellar grain are 359 and 365.5 kJ/mol, respectively. The feature of fracture surface of the Widmanstätten lath structure is transgranular cleavage fracture. The characteristic of fracture surface of the lamellar grain structure is ductile-looking when compared with the Widmanstätten lath structure. The microstructural instability is responsible for the failure of both tested microstructures of the Ti–40Al–10Nb alloy.

Keywords: Titanium aluminides; Niobium; Rolling; Microstructure; Creep

1. Introduction

Owing to the low density and superior high-temperature properties, γ-TiAl based intermetallic alloys have become promising materials for applications in aerospace and automotive industries [1,2]. Nevertheless, the inherent poor ductility and fracture toughness of TiAl alloy at ambient temperature restrict its industrial application. The ductility and fracture toughness can be improved by addition of alloying elements and thermomechanical treatment. The development of TiAl alloys that can be manufactured by conventional processes is necessary. Recently, γ-TiAl alloys produced with the addition of β-stabilizing elements, such as Nb, have been studied [3–5]. These β-containing TiAl alloys have improved room-temperature ductility and high-temperature formability [6]. Furthermore, an investigation by Appel et al. [7] indicates that γ-TiAl alloy with high Nb contents could be extruded as a rod with an extrusion ratio of 10:1. However, the Al content in most TiAl–Nb alloys reported in literatures is above 45 at.%. TiAl alloys with a high Nb content in the Al range between 40 and 45 at.% have been seldom studied.

In this study, the original concept of developing the β-containing Ti–40Al–10Nb alloy is derived from the improvement of ductility of Ti_3Al alloys by adding large amounts of Nb [8]. Our previous research shows that the Ti–40Al–10Nb intermetallic alloy could be processed by hot rolling, and that the alloy microstructure also could be controlled by heat treatment [9]. In addition, the phase characterization of the hot-rolled alloy between 1000 and 1200 °C has been investigated [10]. For high temperature applications, the properties of the alloy, such as creep, must be characterized. Accordingly, this study is to investigate the creep behavior of the hot-rolled Ti–40Al–10Nb alloy, as well as the microstructural effects on the creep deformation.

2. Experimental procedures

Alloys with a nominal composition of Ti–40Al–10Nb (at.%) were prepared in a non-consumable electrode arc remelting furnace under argon protection. The button specimens were remelted and inverted at least 10 times to ensure its homo-

* Corresponding author. Tel.: +886 2 27365527/23634097; fax: +886 2 23634562.
E-mail addresses: d91527003@ntu.edu.tw (C.-J. Zhan), chkoo@ntu.edu.tw (C.-H. Koo).

0921-5093/$ – see front matter © 2006 Elsevier B.V. All rights reserved.
doi:10.1016/j.msea.2006.07.132

geneity. The melts were cast into ingots with the size of 65 mm × 25 mm × 16 mm, and then processed by hot rolling at 1200 °C with a reduction of 40% and followed by air cooling. After the process of hot rolling, the sheets were heated at 1350 °C for 30 min or at 1220 °C for 30 min, and than air cooled to obtain the structure of Widmanstätten lath or lamellar grain, respectively. Both types of sheets were further annealed at 1000 °C for 2 h and air cooled. Microstructures were observed in a scanning electron microscope (SEM) using back-scattered electron imaging (BSE). Tensile creep tests were performed by a constant load creep machine with a lever arm ratio of 20:1 and a furnace with three heating zones (manufactured by Applied Test Systems Inc., Butler, PA). The extension of specimen was measured by a linear variable differential transformer mounted on the specimens, and the gauge dimensions of the specimens were 12 mm × 3 mm × 2 mm. The creep tests were conducted in air for the temperature of 750 °C under the constant stress between 160 and 240 MPa. The deformation substructure and the fracture surface of the crept specimens were examined by a transmission electron microscopy and a scanning electron microscopy.

3. Results and discussion

3.1. Microstructure of Ti–40Al–10 alloy

Fig. 1(a)–(c) show SEM back-scattered electron images and TEM bright field image of the as-cast and the hot-rolled Ti–40Al–10Nb alloy. Fig. 1(a) presents that the microstructure of the as-cast Ti–40Al–10Nb alloy is composed of gray Widmanstätten laths and dark γ phases in a white B2 matrix. The microstructure of the alloy resembles the microstructure of typical as-cast Ti_3Al–Nb alloys, except the presence of the γ phases. Similar to the phase transformations found for the Ti_3Al–Nb alloys, the solidification process of the Ti–40Al–10Nb alloy follows the transformation sequence of $L \rightarrow L+\beta \rightarrow \beta \rightarrow \beta+\alpha \rightarrow \beta+\alpha+\gamma$. When the alloy is cooled through the two phase region of β + α, the α phase precipitates from β matrix through the procedure of Widmanstätten precipitation. Subsequently, when the alloy is further cooled to the three phase region of β + α + γ, the γ phase can form in three different ways: (1) the γ phase precipitates from the Widmanstätten α laths through an eutectoid reaction to form a lamellar structure of alternate plates of γ and α phases, (2) the γ phase precipitates from the β matrix by homogeneous nucleation, and (3) the γ phase precipitates at the interfaces between Widmanstätten laths and the β matrix via heterogeneous nucleation to form a microstructure of granular γ phase. The precipitation of the γ phase in these three different ways can be observed in the Fig. 1(b). The literature reports that both α and β phases are transformed into ordered structures during cooling [11]. In this paper, the ordered α and β phase are referred to as "α_2 phase" and "B2 phase", respectively. Furthermore, the ω phase forms when the B2 phase is further cooling to a lower temperature [12]. The mechanism of the B2 → ω phase transformation is diffusionless without any fluctuation of chemical composition. Hence, the ω phase cannot be observed in SEM back-scattered electron images. The B2 phase has an ordered bcc structure (CsCl structure). The ω phase formed from the ordered B2 has a $B8_2$ type hexagonal structure. The α_2 phase has a $D0_{19}$ type hexagonal structure, while the γ phase has an $L1_0$ type face-centered tetragonal structure. Fig. 1(c) presents the microstructure of the alloy after hot rolling

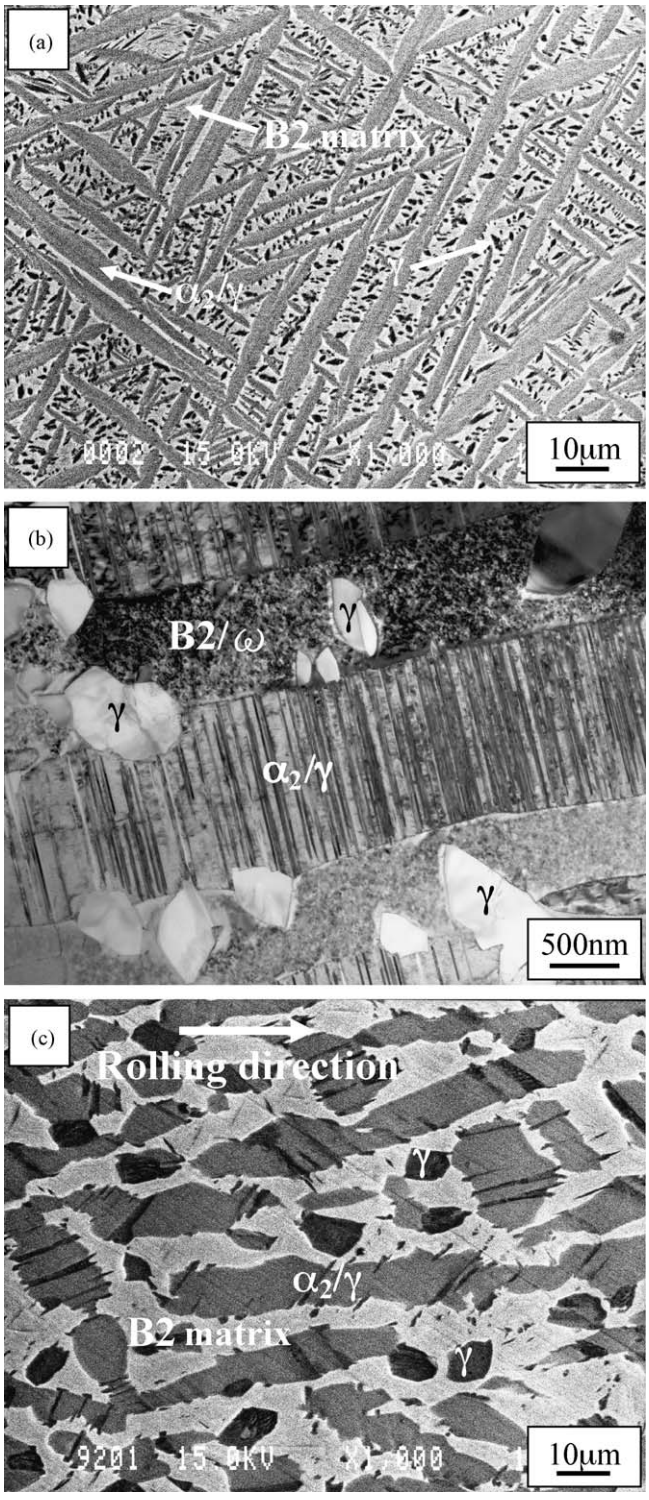

Fig. 1. (a) SEM back-scattered electron image; (b) TEM bright field image of the as-cast Ti–40Al–10Nb alloy; (c) SEM back-scattered electron image of the Ti–40Al–10Nb alloy after hot rolling at 1200 °C with a reduction of 40%.

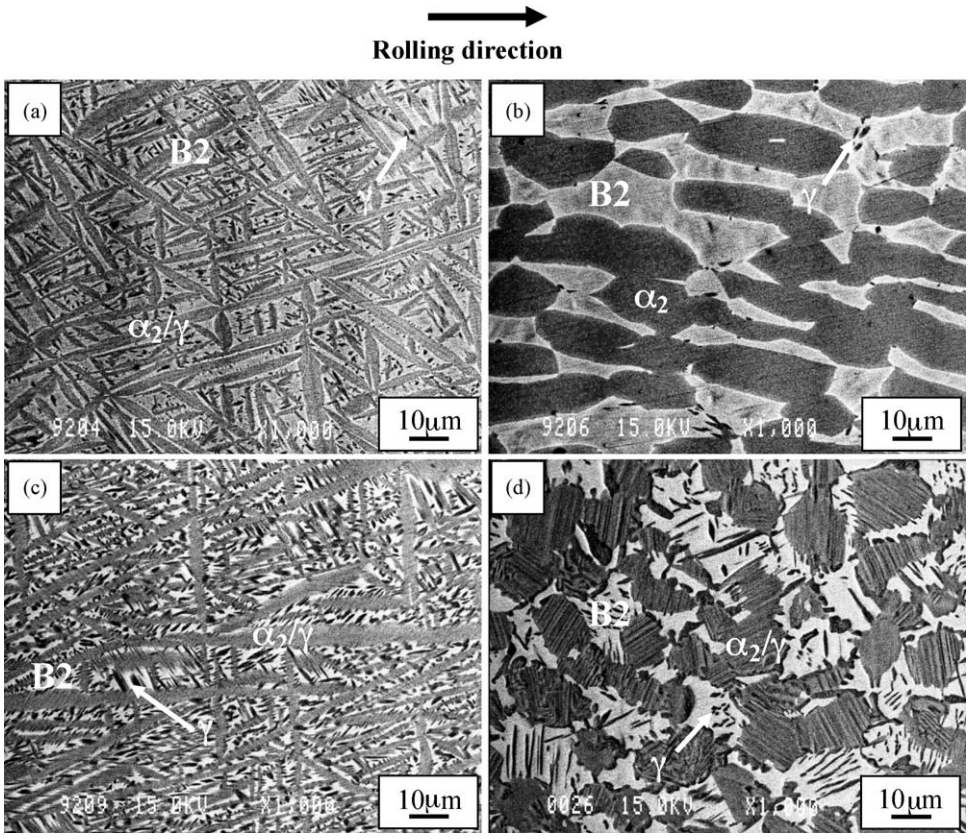

Fig. 2. SEM back-scattered electron images showing the results of the hot-rolled Ti–40Al–10Nb alloy after heat-treated at (a) 1350 °C for 30 min; (b) 1220 °C for 30 min; (c) and (d) the further annealing at 1000 °C for 2 h.

at 1200 °C with a reduction of 40%. The figure reveals that the needle-like Widmanstätten laths are coarsened and elongated along the rolling direction after hot-rolling. In addition, the γ phase originally in Widmanstätten laths has grown into the B2 matrix by discontinuous coarsening, as described by Yu and Koo [9].

Fig. 2 shows BSE images of the microstructure of the hot-rolled Ti–40Al–10Nb alloy after different heat treatments. Fig. 2(a) shows that after annealing at 1350 °C for 30 min in single phase region of β and than followed by air cooling, a microstructure of Widmanstätten laths with a small volume fraction of γ precipitates in the B2 matrix is obtained. While after annealing at 1220 °C for 30 min in two phase region of β + α and then air cooling, a microstructure of α_2 phase with some precipitated γ phase in the B2 matrix is obtained (Fig. 2(b)). Fig. 2(c) and (d) show the microstructure of the heat-treated alloy after further annealing at 1000 °C for 2 h. The subsequent heat treatment is used to further precipitate the γ phase and to ensure the equilibrium of phase composition. Fig. 2(c) reveals that after annealing at 1000 °C, more granular γ phase precipitates in the B2 matrix are present. Similarly, in the sample with α_2 and γ phases (Fig. 2(b)), the α_2 phase changes to the α_2/γ lamellar structure, while the needle-like γ phase originally found in the B2 matrix becomes longer, as shown in Fig. 2(d). The microstructures of samples selected for the creep tests consists Widmanstätten lath (Fig. 2(c)) and a lamellar grain (Fig. 2(d)).

3.2. Creep behavior

Fig. 3 plots the typical creep curves of both tested structures of Ti–40Al–10Nb alloy at 750 °C. The figure clearly presents that

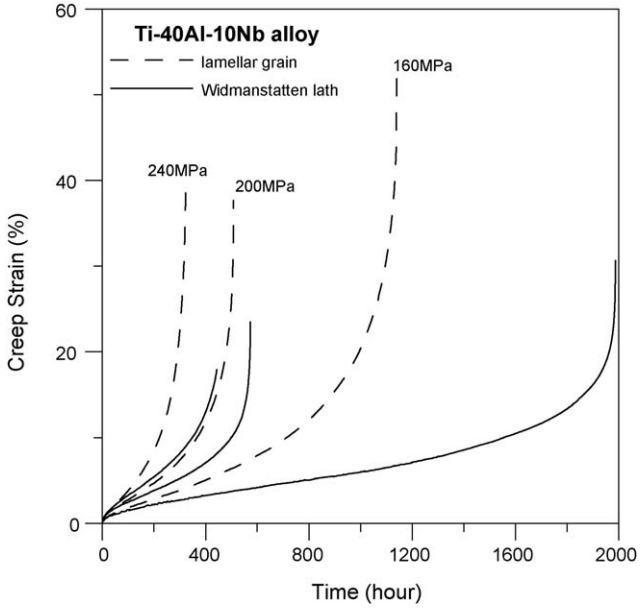

Fig. 3. Creep strain vs. time for the creep test of Ti–40Al–10Nb alloy conducted at 750 °C, and under the constant stress between the range of 160–240 MPa.

the Widmanstätten lath microstructure is more creep resistant than that of the lamellar grain microstructure, which becomes more pronounced with decreasing stress. The accumulated strain before fracture of the β-containing alloy is found to exceed those of nearly lamellar TiAl alloy tested under similar conditions [13]. Because the B2 phase has an open bcc structure, it is expected to be soft and more easily deformed as compared to the α_2 and γ phase at elevated temperature. Therefore, the high creep fracture strain is correlated with the presence of the B2 phase. In this study, the structure of Widmanstätten lath and lamellar grain of Ti–40Al–10Nb alloy are quite similar to those of the transformed β and duplex $\alpha_2 + \beta$ structures found in a Ti_3Al–Nb alloy [14], except for the existence of γ phases. According to Huang and Loretto, the transformed β structure has a better creep resistance due to a shorter dislocation slip length when compared with the duplex $\alpha_2 + \beta$ structure. Therefore, in all the test conditions, the structure of Widmanstätten lath possesses a higher creep resistance than the lamellar grain one also could be explained by the short mean free path of dislocation slip. In addition, seen from the viewpoint of microstructural influence, because the creep deformation constrained by the dense Widmanstätten laths is more than that constrained by the equiaxed lamellar grains, the creep resistance of the Widmanstätten lath structure is higher. The strengthening effect of the dense Widmanstätten lath in the Ti–40Al–10Nb alloy resembles that of the high-aspect-ratio fiber in the TiAl composites [15].

Fig. 4 is a representative creep curve, plotted as creep rate against creep strain, for the Ti–40Al–10Nb alloy with the lamellar grained microstructure deformed at 750 °C and under 200 MPa. As shown in the figure, the characteristics of the curve are the very limited secondary creep region and the prominent range of tertiary creep. Accordingly, the creep response of the alloy is closely related to the tertiary creep. Furthermore, the figure reveals that the primary and the secondary creep strains in proportions to the whole creep strain are as low as 5%. The minimum creep range is around 2–3.5%. The creep curve of the alloy shows a minimum creep region, instead of a steady-state creep region. The reason for this result remains unclear. The reports in the literature offer two possible explanations about the origin of the lack of steady-state creep. Lu et al. [16] attribute the absence of steady-state creep to the lack of a constant dislocation structure, such as a subgrain wall, in ordered alloys. Xia et al. [17] demonstrated that oxidation may accelerate the propagation of cracks in a Ti–46.5Al–2.5V–1Cr alloy during creep, and reduces the effective cross-sectional area, causing the early initiation of the tertiary stage, and the consequent disappearance of the steady state. Their experimental results reveal that the specimens tested in a vacuum show a long steady state whereas those tested in air display only a minimal creep rate.

Fig. 5 shows the microstructure of lamellar grain in a creep test that is interrupted during secondary creep stage with a creep strain of 2.7%, which reaches the minimum creep stage of the alloy. Therefore, the deformation process of the secondary creep may be assessed by the observed microstructure. Fig. 5(a) reveals that among the B2, γ and ω phases, the B2 phase has the highest dislocation density. The dislocations in the B2 are uniformly distributed, and a subgrain structure is not observed. In γ phase few dislocations are present; while almost no dislocations exist in the ω phase. In addition, in Fig. 5(b), dislocations and deformation twins are not observed in the α_2/γ lamellar structure, indicating that the α_2/γ lamellar grain is also not the major phase for creep

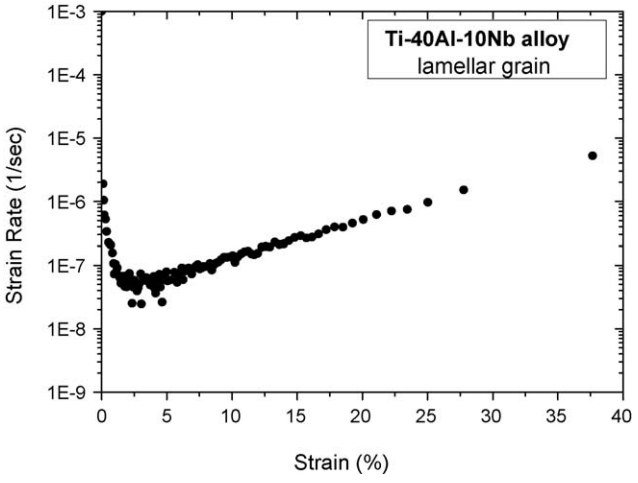

Fig. 4. The strain rate vs. strain for the structure of lamellar grain of the Ti–40Al–10Nb alloy tested at 750 °C/200 MPa.

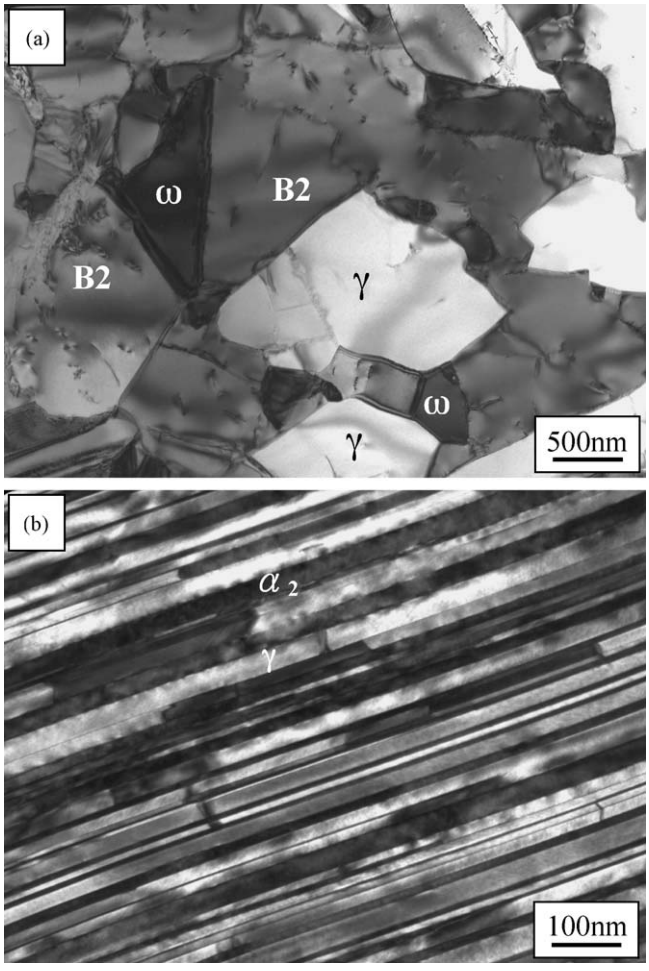

Fig. 5. The TEM bright field image showing (a) the deformed structure of the B2 matrix; (b) the lamellar structure, both after 2.7% strain at 750 °C/200 MPa.

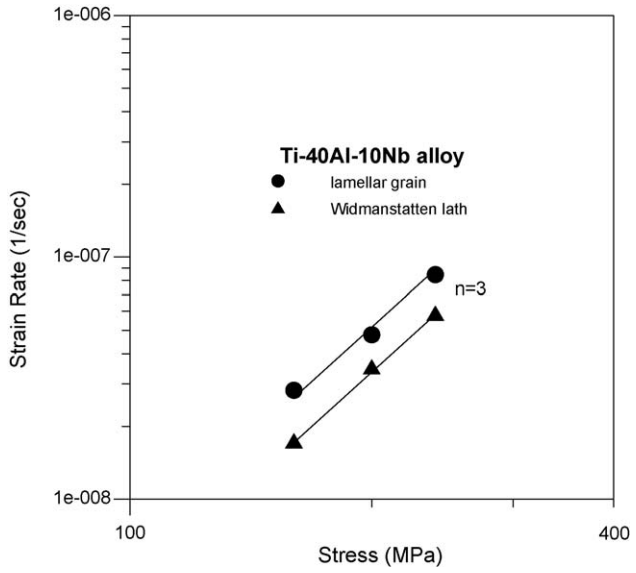

Fig. 6. Minimum creep rate as a function of the stress for the tested Ti–40Al–10Nb alloys of different structures.

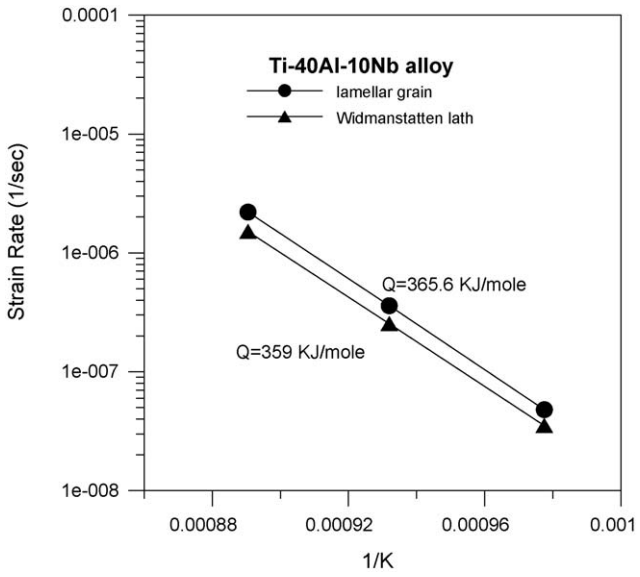

Fig. 7. Temperature dependence of the minimum creep rate for the Ti–40Al–10Nb alloys of two different structures at 200 MPa.

deformation during secondary creep. Therefore, the deformation of the Ti–40Al–10Nb alloy for the secondary creep stage mainly converges in the B2 phase. Fig. 5 clearly presents that the ordered Ti–40Al–10Nb alloys do not show any constant dislocation structure during secondary creep stage. Accordingly, the result of this study is in agreement with those of Lu et al. On the other hand, in respect of the interaction between creep and oxidation, no conclusive proofs are shown in this study but further study seems necessary.

Fig. 6 plots the stress dependence of the minimum creep rate for two different structures of Ti–40Al–10Nb alloy. A stress exponent of three has been estimated for these two structures, suggesting that the creep mechanism of the alloy is dislocation

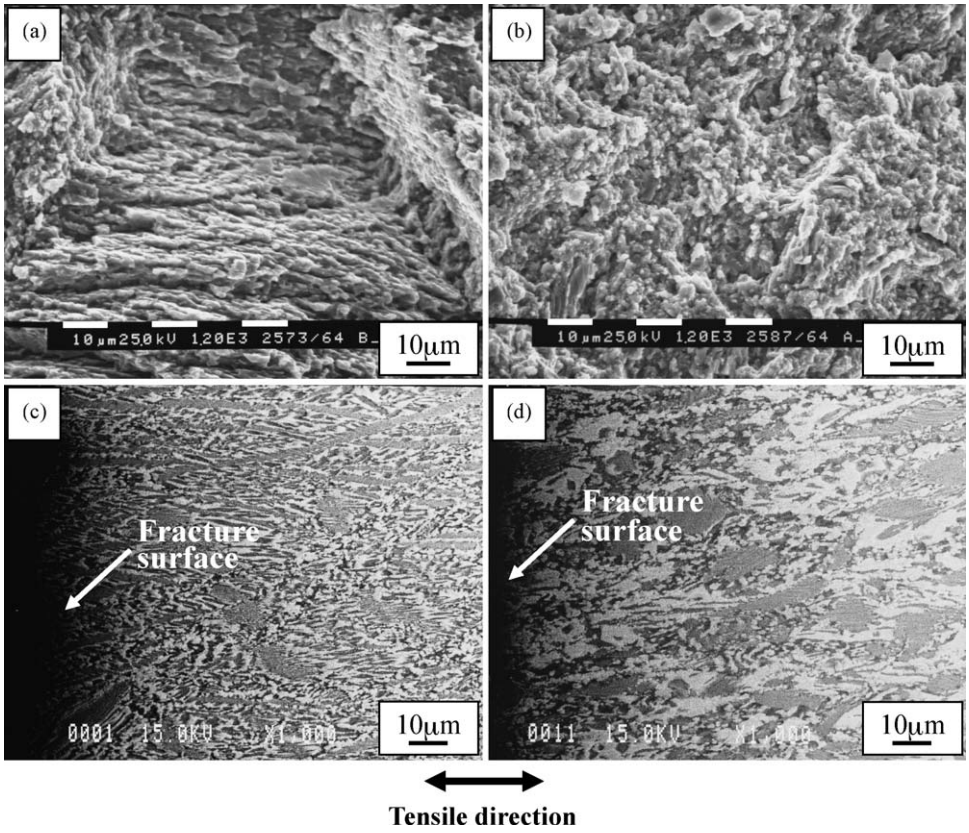

Fig. 8. Creep fractured surface for the structure of the (a) Widmanstätten lath; (b) lamellar grain at 750 °C/200 MPa; microstructure close to the fracture surface for the structure of the (c) Widmanstätten lath; (d) lamellar grain after creep test at 750 °C/200 MPa.

glide and climb [18]. According to the stress exponent estimated and the TEM observation of Fig. 5, the creep behavior for this alloy is governed by a mechanism of dislocation motion in the B2 matrix. The creep deformation is mainly contributed by gliding and climbing of dislocations in the B2 phase, while dislocation climb is the rate-controlling for creep. The dislocation climb is a thermal activated process, which corresponds to the activation energy of lattice self-diffusion. Fig. 7 plots the temperature dependence of the minimum creep rate for the different structures of the Ti–40Al–10Nb alloy. The calculated activation energy are 359 and 365.6 kJ/mol for the structure of Widmanstätten lath and lamellar grain, respectively. The calculated values of activation energy for the two test structures are quite close to the activation energy of Ti self-diffusion in the β phase (∼353 kJ/mol) [6]. Consequently, it is conceivable that the minimum creep rate is controlled by lattice self-diffusion of the B2 phase.

3.3. Fracture analysis

Fig. 8 displays selected fractographys of the two tested microstructures of the Ti–40Al–10Nb alloy after the creep test. Fig. 8(a) and (b) are the fracture surface for the structure of Widmanstätten lath and lamellar grain at 750 °C and under 200 MPa, respectively. The fracture surface is subject to oxidation and covered with a heavy oxide layer. Fig. 8(c) and (d) show the microstructures of two types of different crept samples in the gauge length of test specimens close to the fracture surface. The tensile direction, which is the same as the rolling direction, is indicated in the figures. As seen from Fig. 8(a) and (c), the characteristic of fracture surface of the Widmanstätten lath structure is transgranular cleavage fracture and the cracking proceeds by traversing the Widmanstätten laths as well as the B2 matrix. Conversely, the feature of fracture surface of the lamellar grain structure as compared to the Widmanstätten lath structure is ductile-looking event though the cracking also propagates by directly crossing the lamellar grains and the B2 matrix, as shown in Fig. 8(b) and (d). The observation of the fracture surface for the two tested microstructures of the Ti–40Al–10Nb alloy indicates that the morphology of the α_2 phase, such as the dense Widmanstätten laths and the equiaxed lamellar grains, evidently affects the look of fracture surface of the alloy. Because the deformation of the B2 phase restricted by the equiaxed lamellar grains is less than that restricted by the dense Widmanstätten laths during creep, the fracture surface of the lamellar grain structure shows a ductile-looking character.

During tertiary creep, the strain rate is rapidly increased along with increasing accumulated strain, resulting in unstable deformation and leading to the damage of alloys. The accelerating strain rate is commonly connected with microstructural instabilities or the formation and coalescence of voids or cracks [19]. In this present study, no cavities or voids have been observed in the crept samples through the SEM examination, but the predominantly microstructural changes of the crept specimens are observed near the fracture surface, especially after long-term creep test. In the Fig. 9, arrows indicate the microstructural changes. As seen from Fig. 9(a), some parts of the Widmanstätten lath are dissolved into the B2 matrix. The microstructures of fine grains are also observed in Fig. 9(a). The same phenomenon applies to the lamellar grain structure, as shown in Fig. 9(b). According to our previous study [20], the $\alpha_2 \rightarrow \beta$ transformation is observed to take place at relatively high temperature (>1300 °C). In this study, however, the transformation of $\alpha_2 \rightarrow \beta$ is found to occur at the temperature of 750 °C, suggesting that the transformation is induced by stress. Likewise, the presence of fine grains microstructures is believed to be related to the creep-induced process. Therefore, from the microstructural observation of the crept sample, the result clearly reveals that the reason for the creep fracture of the two test microstructures is identical. The microstructural instability is responsible for the damage of the Ti–40Al–10Nb alloy at a creep temperature.

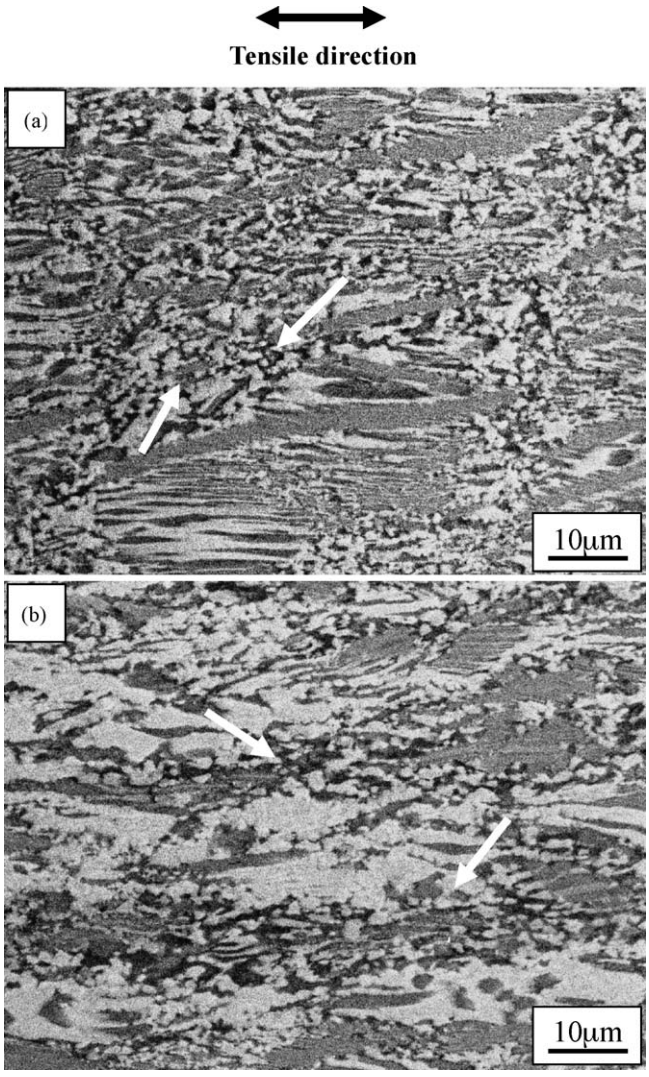

Fig. 9. Microstructural changes for the structure of the (a) Widmanstätten lath; (b) lamellar grain close to the fracture surface after tensile creep deformation at 750 °C/200 MPa.

4. Conclusions

(1) The microstructure of the as-cast Ti–40Al–10Nb alloy is composed of the gray Widmanstätten laths and the dark

γ phase in a white B2 matrix. After annealing at 1350 °C in single phase region of β, a microstructure of the Widmanstätten laths with few γ phases in the B2 matrix is obtained. While annealing at 1220 °C in two phase region of β + α, the microstructure of the sample changes to the α_2 phase with some precipitated γ phases in B2 matrix.

(2) The creep resistance of the Widmanstätten lath microstructure is quite high compared with that of lamellar grain microstructure. The creep response of the Ti–40Al–10Nb alloy is closely related to the tertiary creep. The creep curve of the alloy does not exhibit an extended steady-state region, which appears to be related to the lack of a subgrain structure of dislocations. TEM observation shows that the creep deformation of the alloy primarily converges in the B2 phase during secondary creep stage. A stress exponent of three measured for the studied two structures of Ti–40Al–10Nb alloy suggests that the creep mechanism of the alloy is dislocation glide and climb. The calculated activation energy are 359 and 365.6 kJ/mol, for the structure of Widmanstätten lath and lamellar grain, respectively.

(3) The feature of fracture surface for the Widmanstätten lath structure is transgranular cleavage fracture. The characteristic of fracture surface of the lamellar grain structure is ductile-looking when compared with the Widmanstätten lath structure. Microstructural observation of the crept specimen demonstrates that microstructural instability is responsible for the damage of both tested structures of the Ti–40Al–10Nb alloy.

References

[1] H. Clemens, H. Kestler, Adv. Eng. Mater. 2 (2000) 551.
[2] T. Tetsui, Mater. Sci. Eng. A329 (2002) 582.
[3] W. Zhang, G. Chen, Y. Wang, Z. Sun, Scr. Mater. 28 (1993) 1113.
[4] J.D.H. Paul, F. Appel, R. Wanger, Acta Mater. 46 (1998) 1075.
[5] C.T. Yang, Y.C. Lu, C.H. Koo, Intermetallics 10 (2002) 161.
[6] J.G. Wang, T.G. Nieh, Intermetallics 8 (2000) 737.
[7] F. Appel, M. Oehring, R. Wagner, Intermetallics 8 (2000) 1283.
[8] C.H. Ward, Int'l Mater. Rev. 38 (1993) 79.
[9] T.H. Yu, C.H. Koo, Mater. Sci. Eng. A239 (1997) 694.
[10] T.H. Yu, C.H. Koo, Scr. Mater. 39 (1998) 915.
[11] G. Shao, P. Tsakiropoulous, A.P. Miodowinik, Intermetallics 3 (1995) 315.
[12] L.A. Bendersky, W.J. Boettinger, B.P. Burton, F.S. Biancaniello, Acta Mater. 38 (1990) 931.
[13] W.J. Zhang, G.L. Chen, F. Appel, T.G. Nieh, S.C. Deevi, Mater. Sci. Eng. A315 (2001) 250.
[14] C. Huang, M.H. Loretto, Mater. Sci. Eng. A192 (1995) 722.
[15] S.L. Kampe, J. Christodoulou, C.R. Feng, L. Christodoulou, D.J. Michel, Acta Mater. 46 (1998) 2881.
[16] M. Lu, K.J. Hemker, Acta Mater. 45 (1997) 3573.
[17] K. Xia, X. Wu, J. Zhang, Intermetallics 11 (2003) 325.
[18] J. Cadek, Creep in Metallic Materials, Elsevier, Amsterdam, Netherlands, 1988.
[19] J. Beddoes, W. Wallace, L. Zhao, Int'l. Mater. Rev. 40 (1995) 197.
[20] T.H. Yu, PhD dissertation, National Taiwan University, Taipei, Taiwan, 1998.